Cell Reports
Physical Science

CellPress
OPEN ACCESS

Article

Managing gas and ion transport in a PTFE fiber-based architecture for alkaline fuel cells

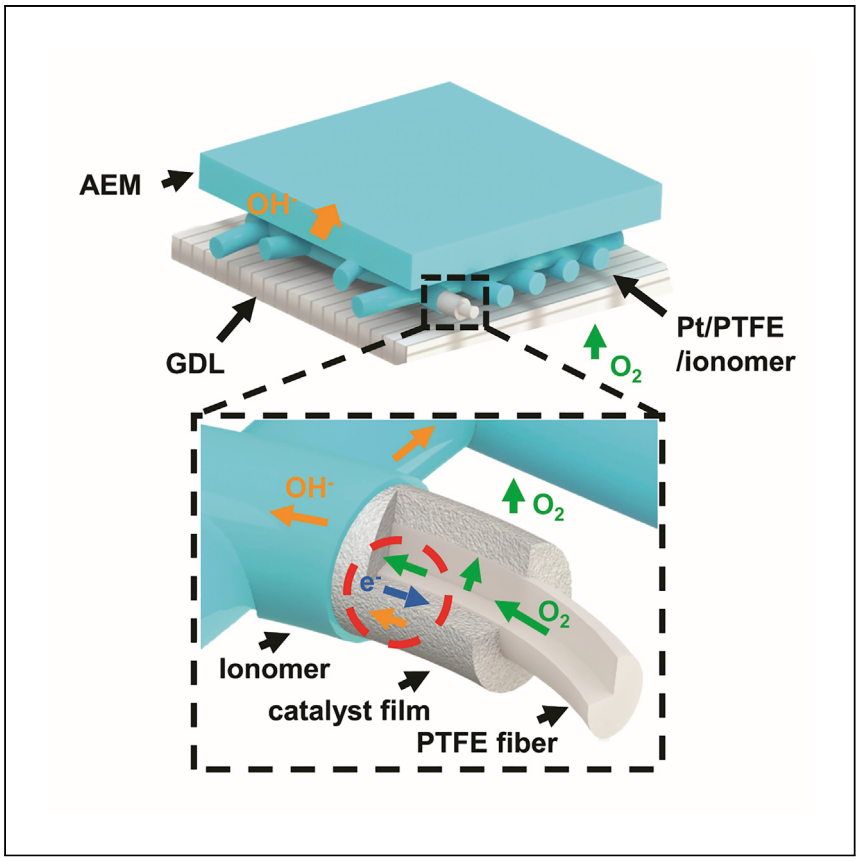

Yan et al. employ a fiber-based architecture for alkaline fuel cells, simplifying the analysis of mass transport in the catalyst layers. Using this design, ion and gas transport are found to limit fuel cell performance at low and high ionomer loadings, respectively.

Zhifei Yan, Michael Colletta, Akshay Venkatesh, ..., Lena F. Kourkoutis, Héctor D. Abruña, Thomas E. Mallouk

mallouk@sas.upenn.edu

Highlights

PTFE fiber-based catalyst layers for oxygen reduction electrode in alkaline fuel cells

Strong dependence of fuel cell performance on ionomer loading

Gas and ion transport limits fuel cell performance at different ionomer loadings

Inductive loop in impedance spectra relates to oxygen transport

Yan et al., Cell Reports Physical Science 3, 100912
June 15, 2022
https://doi.org/10.1016/j.xcrp.2022.100912

Cell Reports
Physical Science

CellPress
OPEN ACCESS

Article

Managing gas and ion transport in a PTFE fiber-based architecture for alkaline fuel cells

Zhifei Yan,[1] Michael Colletta,[2] Akshay Venkatesh,[1] Yao Yang,[3] Jeremy L. Hitt,[1] Jeffrey M. McNeill,[1] Lena F. Kourkoutis,[2,4] Héctor D. Abruña,[3] and Thomas E. Mallouk[1,5,*]

SUMMARY

Hydrogen fuel cells are needed for long-haul, heavy-duty transportation applications that are beyond the range of electric vehicle technology. Recently, advances in membrane science have enabled alkaline fuel cells, which in principle do not require precious metal catalysts, to compete with fuel cells that utilize acidic membranes. Here, we combine cryo-electron microscopy, electrochemistry, and numerical modeling to understand the performance of the cathode of alkaline fuel cells, where oxygen combines with water to make hydroxide anions. We examine the conventional electrode architecture, where catalyst nanoparticles are supported on carbon and surrounded by a thin film of ionomer, with a new architecture of catalyst particles on gas-permeable fluorocarbon fibers. These studies show that the conventional architecture would work more efficiently with ionomers that are more permeable to oxygen. The fiber architecture manages oxygen and ion transport well, but its performance is limited by the activity of the catalyst.

INTRODUCTION

The net-zero carbon economy can be achieved by shifting to renewable energy sources such as solar and wind. The intermittency of these sources requires a robust and efficient means of storing surplus energy in a stable form, which can be converted back to electricity during peak demand.[1,2] While the short-term storage problem can be addressed with lithium-ion batteries, batteries are impractical for long-term (seasonal) storage or for long-haul transportation applications where cost and long charging times currently preclude their use. H_2-O_2 fuel cells hold great promise for both applications since they can convert chemically stored energy to electricity with high efficiency. Among the various kinds of fuel cells, alkaline exchange membrane fuel cells (AEMFCs) enable the use of earth-abundant electrocatalysts and could potentially rival their acidic counterpart, proton exchange membrane fuel cells (PEMFCs) in efficiency, stability, and cost.[3–8]

Many efforts have focused on designing fuel cell electrocatalysts with high activity and durability, and on advancing our understanding of the interfacial charge transfer kinetics of hydrogen oxidation and oxygen reduction. On the other hand, the problem of gas and ion transport represents an important and complex problem at the system level that is not well understood. Rotating disk electrode (RDE) voltammetry is generally used for fast catalyst screening, as it offers a relatively simple and precise control of convective flow for mass transport. At the RDE, the effects of mass transport and electrode kinetics can be separately quantified by using the *Koutecky-Levich* equation. This problem becomes more complicated when one switches to

[1]Department of Chemistry, University of Pennsylvania, Philadelphia, PA 19104, USA

[2]School of Applied and Engineering Physics, Cornell University, Ithaca, NY 14853, USA

[3]Department of Chemistry and Chemical Biology, Cornell University, Ithaca, NY 14853, USA

[4]Kavli Institute at Cornell for Nanoscale Science, Cornell University, Ithaca, NY 14853, USA

[5]Lead contact

*Correspondence: mallouk@sas.upenn.edu

https://doi.org/10.1016/j.xcrp.2022.100912

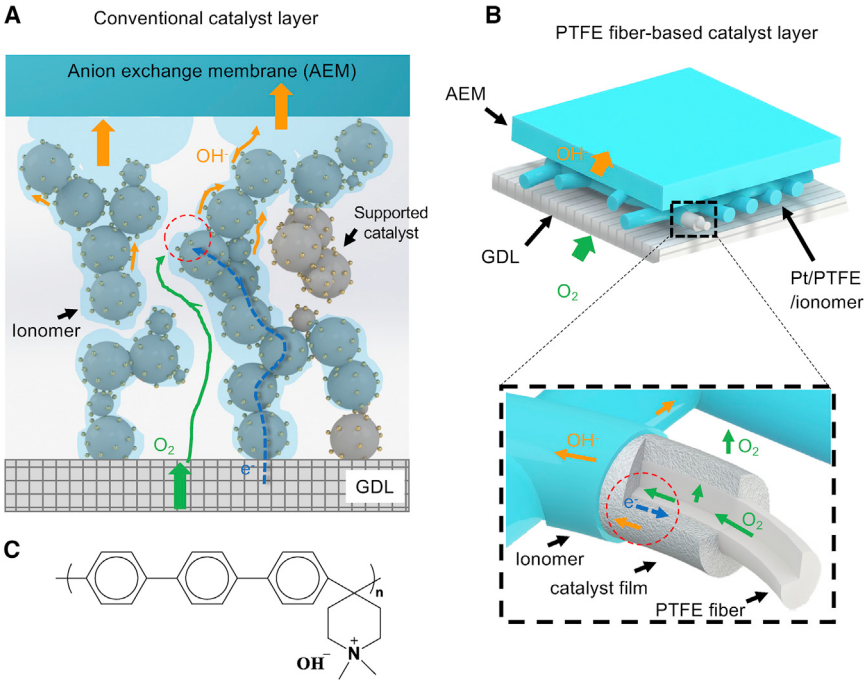

Figure 1. Schematics of mass transport in different electrode architectures

(A and B) (A) Conventional catalyst layer and (B) PTFE fiber-based catalyst layer for the oxygen reduction reaction (ORR) electrode in alkaline fuel cells. In the former case, gas (green), electron (blue), and hydroxide ion (orange) are transported by the gas pores, electronically conducting support, and ionomer, respectively. In the latter, the PTFE fibers provide an additional transport pathway for the O_2 gas due to its high affinity toward nonpolar gases. In both (A) and (B), the red circle denotes a site where electrochemical reactions can happen.

(C) Chemical structure of the AEM and ionomer used in this work,[4] quaternary ammonia poly (N-methyl-piperidine-co-p-terphenyl) (QAPPT).

a fuel cell device in which catalysts coat the ion exchange membrane to form a membrane electrode assembly (MEA).[9–11] Understanding ion and molecule transport in the catalyst layer is a multiscale problem that involves the transport of gaseous reactants in the flow channels and in gas diffusion layers that contain macroscopic pores (>1 μm). The stacking of the catalyst, support, and ionomer creates a network of narrower pores that must balance the diffusion of neutral molecules and the migration of ions, while the microstructure in the catalyst support layer affects transport at the nanometer scale. Mass transport to and from the reaction zone is also an intrinsically multi-phase problem. The catalyst layer consists of a disordered mixture of the solid catalyst and support particles, soft materials such as ionomers, condensed liquid water, and the gaseous reactants and water vapor.

The triple-phase boundary model assumes that the electrochemical reaction occurs in regions where the catalyst/support, ionomer, and gas pores meet, providing the predominant electronic, ionic, and gas transport pathways, respectively (Figure 1A). While the validity of this model has been confirmed at the sub-micrometer length scale,[12,13] the governing principles in the molecular and nanoscale regimes remain unclear. For example, supports abundant in micropores (~4 nm) have been shown to enhance catalyst activity because the catalyst nanoparticles deposited inside these pores are free of ionomer on their surface, and thus the poisoning effect from ionomer. This leaves the ionic conduction pathway within the micropores of the support as an open question.[14] The supramolecular structure and behavior of ionomers also

change dramatically in confinement, i.e., when the dimensions change from the micron to nanometer regime,[15–17] the latter being the typical thickness of the ionomer films in the catalyst layer.[18] The effect of ionomer on oxygen transport near the catalyst surface has been proposed to limit the performance of PEMFCs at low catalyst loadings, due to the oxygen transport resistance through ionomer films.[17,19]

Correlating microscopic transport theory with the macroscopic performance of fuel cells is a long-standing challenge due to our lack of detailed knowledge of the catalyst layer structure and its individual components. Physical characterization of the disordered catalyst/support/ionomer microstructure has been performed by using techniques such as the nanoscale X-ray computed tomography (nano-CT)[20] and cryogenic scanning transmission electron microscopy (cryo-STEM),[21] generating useful information at certain length scales. In this context, novel designs of the catalyst layer that can offer better control of the local structure would be beneficial. For example, it is possible to construct an ionomer-free architecture in which a nanostructured thin film (NSTF) catalyst layer serves to conduct both the electrons and ions.[22] Recently, Sargent et al have designed such a catalyst/ionomer heterojunction to decouple the transport pathways for electrons, ions, and gas molecules in a gas-fed CO_2 electrolyzer, achieving ~1.2 A/cm^2 current density for the conversion of CO_2 to ethylene.[23,24]

Designing catalyst layers with more controllable architectures should facilitate the study of molecular and ionic transport processes and their impact on fuel cell performance. In this work, we studied the effect of ionomer loading on transport in conventional catalyst layers (Figure 1A). Cryogenic transmission electron microscopy (Cryo-TEM) images, electrochemical impedance spectroscopy (EIS) results, and fuel cell performance tests indicated that higher loading leads to thicker ionomer films and higher diffusion resistance to O_2 gas, while ionic transport becomes rate-limiting at lower ionomer loading. We then explored mass transport in a polytetrafluorethylene (PTFE) fiber-based architecture in which a thin Pt or Ag catalyst film was sputtered onto a porous PTFE membrane (Figure 1B), which was used as the oxygen reduction reaction (ORR) electrode for AEMFCs. The PTFE fiber was chosen for its high affinity toward nonpolar gases such as oxygen, and it thus serves as both an oxygen gas transport medium and a support for the catalyst film. A much lower optimal ionomer loading was found for the Pt/PTFE architecture compared with the conventional structure. EIS measurements combined with numerical modeling revealed that the transport of oxygen gas was significantly impeded at higher ionomer coverage beyond a certain loading threshold, while lower ionomer loading limits the performance because of the lack of efficient ionic transport pathway.

RESULTS

Effects of ionomer coverage in the conventional catalyst layer

Conventional catalyst layers were made by spraying homogenized catalyst inks containing high surface area carbon-supported Pt nanoparticles, anion exchange membrane (AEM) ionomers, and n-propanol solvent. The as-formed catalyst layer on the AEM consists of aggregates of the supported catalysts and ionomers, with pores in-between for gas transport (Figure 1A). We first compared two ionomer loadings, 18.8 μL/cm^2 and 7.5 μL/cm^2 (corresponding to 4:1 and 10:1 supported catalyst: ionomer weight ratio). The structure of the AEM and ionomer, quaternary ammonium poly (N-methyl-piperidine-co-*p*-terphenyl) (QAPPT), for this study is shown in Figure 1C. Cryo-TEM characterization of the catalyst layer formed directly on the sample grid showed platinum nanoparticles, the graphitic carbon support, and the

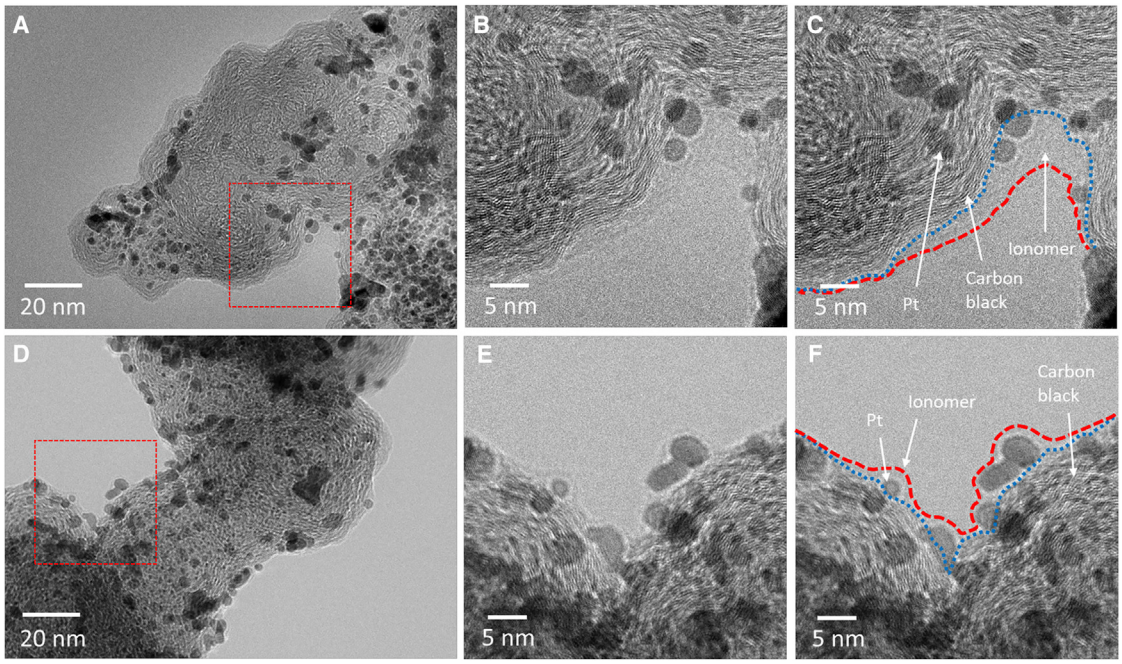

Figure 2. Cryo-TEM characterization of ionomer distribution in catalyst/ionomer composite samples

(A–C) show a sample with high ionomer loading (18.8 μL/cm^2, 4:1 catalyst: ionomer weight ratio).

(D–F) (D) and (E) show a low ionomer loading (7.5 μL/cm^2, 10:1 catalyst: ionomer weight ratio). Geometric areas (4 cm^2) are used to normalize ionomer loadings. Carbon black (blue dotted line) is identified as having a periodic, graphite-like structure, while ionomer (red dashed line, F) shows an amorphous structure around the edges of the catalyst particle.

amorphous ionomers (Figure 2). Thicker and denser ionomer films around the Pt/C aggregates were observed at higher ionomer loading (18.8 μL/cm^2, Figure 2C). The sample with 7.5 μL/cm^2 ionomer loading showed sparser and thinner ionomer films (~1 nm) and thus more exposed Pt catalyst particle surfaces (Figure 2F and S1).

The fuel cell with 18.8 μL/cm^2 ionomer loading achieves much higher power density than the 7.5 μL/cm^2 sample (Figures 3A and 3C). This is due to higher ionic transport resistance because of the interrupted ionic conduction pathway in the latter. The two-electrode EIS spectrum of AEMFCs with the conventional catalyst layer showed a suppressed semicircle (Figure 3B), which possibly includes both charge transfer and gas transport processes.[25] Interestingly, EIS spectra with lower ionomer loading exhibit a primary depressed semicircle and a low-frequency loop at low current densities (Figure 3D), which has been observed previously and ascribed to the electrochemical-chemical-electrochemical (ECE) reaction mechanism of the alkaline ORR.[26] The loop feature was absent in the higher ionomer loading case because it was masked by the diffusion process through the ionomer film.[26] This is possible because at high ionomer loadings, most of the catalyst agglomerates are covered by a thick ionomer film that adds a pressure-independent diffusion barrier to the O_2 transport process, particularly at low catalyst loadings.[11,17] Designing ionomers with high oxygen permeability and ionic conductivity could in principle mitigate this problem, as has already been demonstrated for PEMFCs.[19]

Design of PTFE fiber-based catalyst layers

To achieve more controllable local structures in the catalyst layer, following the design of Garcia de Arquer et al.,[23] we sought to create alkaline fuel cell cathodes

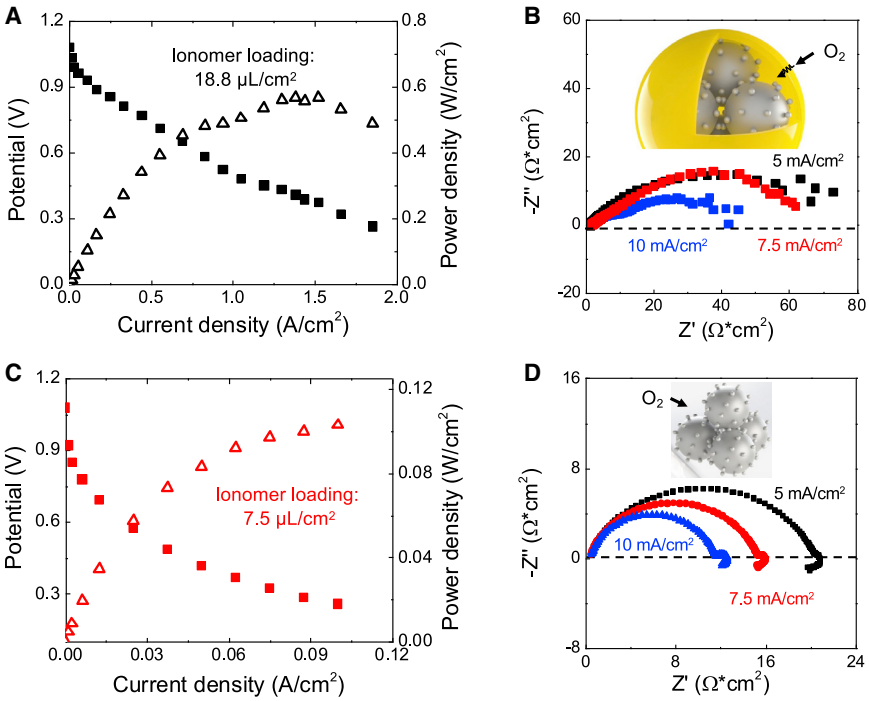

Figure 3. Polarization and power density curves of AEMFCs with conventional catalyst layers

(A–D) (A) With 18.8 and (C) with 7.5 μL/cm^2, ionomer loading (weight loading: 0.1 and 0.04 mg/cm^2, respectively). The corresponding Nyquist plots for (B) 18.8 and (D) 7.5 μL/cm^2 are shown on the right. The inset indicates that higher ionomer loading leads to thicker ionomer films that introduce additional O_2 transport resistance. Tests were done with a conventional catalyst layer, cathode: 0.4 mg metal/cm^2 Pt/C (60 wt%); anode: 0.4 mg metal/cm^2 PtRu/C (60 wt%); AEM (35 μm) and ionomers: QAPPT; the fuel cell was heated at 80°C; humidified H^2 and O^2 gas were fed in with a flow rate 500 mL/min. Solid and open symbols refer to the potential and power density, respectively. Geometric areas (4 cm^2) are used to normalize ionomer loadings, current densities, and power densities.

by sputtering an Ag or Pt catalyst film onto a porous membrane consisting of PTFE fibers, taking advantage of the high affinity of PTFE toward nonpolar gases such as O_2. A nominally 400-nm-thick metal layer was deposited as the catalyst layer (Figures S2 and S3). The anode electrode was kept the same as in the conventional geometry by spraying a homogenized PtRu/C/ionomer ink onto the AEM.

The sputtered Ag and Pt form continuous and dense films along the PTFE fibers, while retaining the porous structure of the original substrate (Figures 4A, 4B, and S3–S5). Interestingly, without adding any ionomer, the Ag/PTFE cathode achieves ~1 A/cm^2 current density and ~170 mW/cm^2 peak power density (Figure 4C), whereas the Pt/PTFE cathode behaves very poorly under the same conditions, <0.1 A/cm^2 and ~15 mW/cm^2 (Figure 4D). This striking difference may arise from the different surface properties of the Ag and Pt films. We hypothesize that the former may effectively act as an ion conductor but the latter cannot. To test this hypothesis, we then sprayed a thin ionomer film onto the Pt-coated PTFE membranes. Adding the same amount of AEM ionomer (75 μL, 31.3 μL/cm^2) as in the conventional MEA to Pt/PTFE leads to much improved fuel cell performance, 0.4 A/cm^2 versus 0.08 A/cm^2 (Figure 5A). In contrast, the polarization and power curves of the Ag/PTFE with and without added ionomer showed similar results (Figure S6). This indicates that the Pt/PTFE electrode requires AEM ionomer to conduct ions.

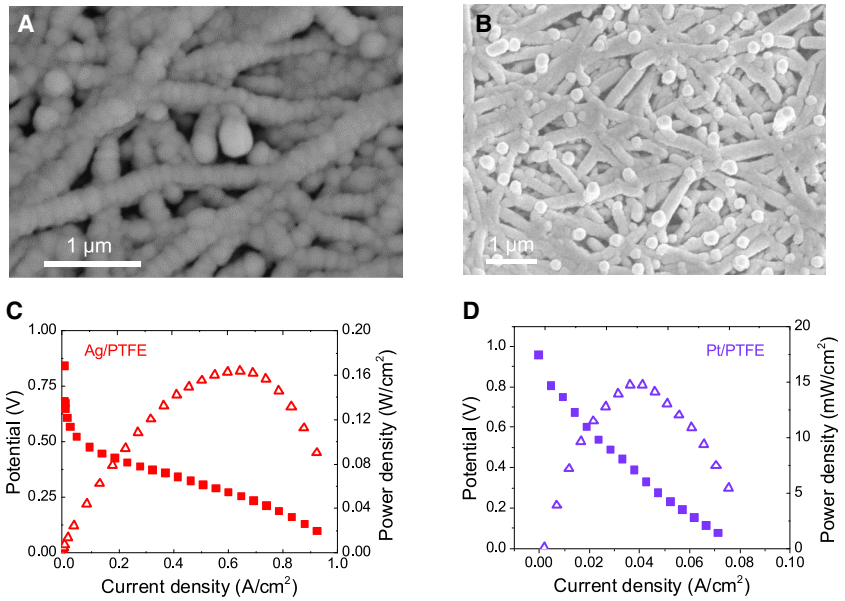

Figure 4. Catalyst/PTFE fiber catalyst layer

(A–D) Top view scanning electron microscope (SEM) images of (A) Ag/PTFE and (B) Pt/PTFE. Polarization and power density curves of the AEMFCs using the (C) Ag/PTFE and (D) Pt/PTFE as the ORR electrode. Cathode: Pt/PTFE or Ag/PTFE catalyst layer, without ionomer; anode: 0.4 mg metal/cm^2 PtRu/C (60 wt%), ionomer was added in a 4:1 catalyst/ionomer ratio (18.8 μL/cm^2 ionomer loading); the fuel cell was heated at 80°C; humidified H_2 and O_2 gas were fed in with a flow rate 500 mL/min. Solid and open symbols refer to the potential and power density, respectively.

In addition to the ~400-nm catalyst layer on the PTFE substrate, an Ag coating was also observed around the much thinner PTFE fibers (Figure S5). Given that this was not seen for the Pt catalyst layer (Figure S4), it appears that Pt and Ag have different affinities for the low-energy PTFE surface, which might be another reason for the drastically different fuel cell performance (Figures 4C and 4D). Replacing the AEM ionomer with the cation exchange ionomer Nafion results in poorer performance (Figure S7). This differs from the previous report of using Nafion and Cu/PTFE for CO_2 electrolysis,[23] where the high current density may involve fast transport of the anions (HCO_3^-, OH^-) in the Nafion film, which shows lower permselectivity in alkaline aqueous (i.e., liquid) electrolytes than in acidic environments.[27] The poorer performance with Nafion ionomer might also be due to the crosslinking between Nafion and the positively charged AEM, which increases the ionic transport resistance at the cathode/membrane interface.

A dramatic impact of the AEM ionomer loading on the fuel cell performance was found for the Pt/PTFE electrodes (Figure 5). Increasing the loading from 0.8 to 2.5 μL/cm^2 increases the limiting current density and peak power density from ~0.1 to >0.8 A/cm^2, and <50 to ~280 mW/cm^2, respectively. A further increase in loading above 2.5 μL/cm^2 leads to lower performance (Figure 5). The metallic loading on the platinized 400-nm-diameter PTFE fibers was measured to be ~1 mg/cm^2, which is about twice as high as in a conventional MEA cathode. Decreasing the thickness of the Pt film to 300 nm resulted in a lower cell performance (Figure S8), which might be caused by increased series resistance. The requirement of high precious metal loading could in principle be mitigated by sputtering a conductive support layer before depositing the thin catalytically active film.

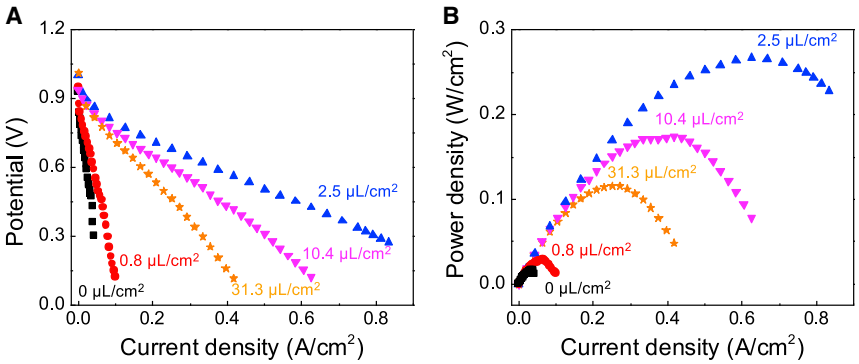

Figure 5. The effects of ionomer loading on fuel cell performance with Pt/PTFE cathodes
(A and B) (A) Polarization curves and (B) power density curves. Other testing conditions are the same as in Figure 4, and can be found in the supplemental experimental procedures. The geometric area of the Pt/PTFE electrodes was 2.4 cm^2.

Mass transport in the PTFE fiber-based catalyst layers

We next explored mass transport in the Pt/PTFE architecture by combining EIS measurements and numerical modeling. Cross-sectional scanning electron microscopy (SEM) images of the catalyst layer showed a Pt coating layer of ~400 nm with a grain size of ~50 nm (Figure 6A). We modeled the Pt/ionomer-coated PTFE fiber in the one-dimensional approximation (Figure 6B). In this model, the cathode consists of a 1-μm porous electrode domain and a 10-μm electrolyte segment. The one-dimensional porous electrode corresponds to a region that, in the two-dimensional domain, contains PTFE, Pt, and ionomer film (Figure 6B). In a mean field sense, the porous electrode thus has the properties of its constituents, namely, gaseous permeability due to the PTFE fibers, electronic conductivity by the Pt film, and ionic conductivity by the ionomer. The electrolyte domain describes ionic transport within the polymer electrolyte. Further discussion on the one-dimensional model is available in Schemes S1 and S2 and Note S1.

We assumed an ECE mechanism for the ORR process in the porous electrode (see supplemental experimental procedures).[26] Two types of boundary conditions were compared, which fixed the concentration of oxygen at the open boundary of the electrode (at x = 0, model 1) or the electrolyte (at x = 11 μm, model 2). The first model represents the conditions in the PTFE fiber-based architecture and the second resembles those with thick ionomer films where the gas must diffuse through the polymer electrolyte for the electrode reaction. The latter case might be encountered in RDE experiments in an aqueous environment even though the ionomer film is usually sub-micrometer in thickness, as discussed below.

The experimental EISs were acquired at low overpotential (high cell voltage, 0.75 V) to minimize interference from the anodic HOR (which, though has larger overpotential in alkaline than acidic conditions, is still orders of magnitude faster than the ORR[28,29]), and thus can be considered as characteristic of the ORR at the cathode. This assumption was further strengthened by using a much larger surface area for the anode than the cathode in the PTFE fiber-based architecture. The experimental spectrum consists of a capacitive semicircle and an inductive loop at high and low frequencies, respectively (Figures 6C and S9), corresponding to the negative and positive imaginary impedance in the Bode plot (Figure 6D). The simulated EIS spectra in model one reproduce the main features of the experimental results, even though the absolute impedance values are about one magnitude off

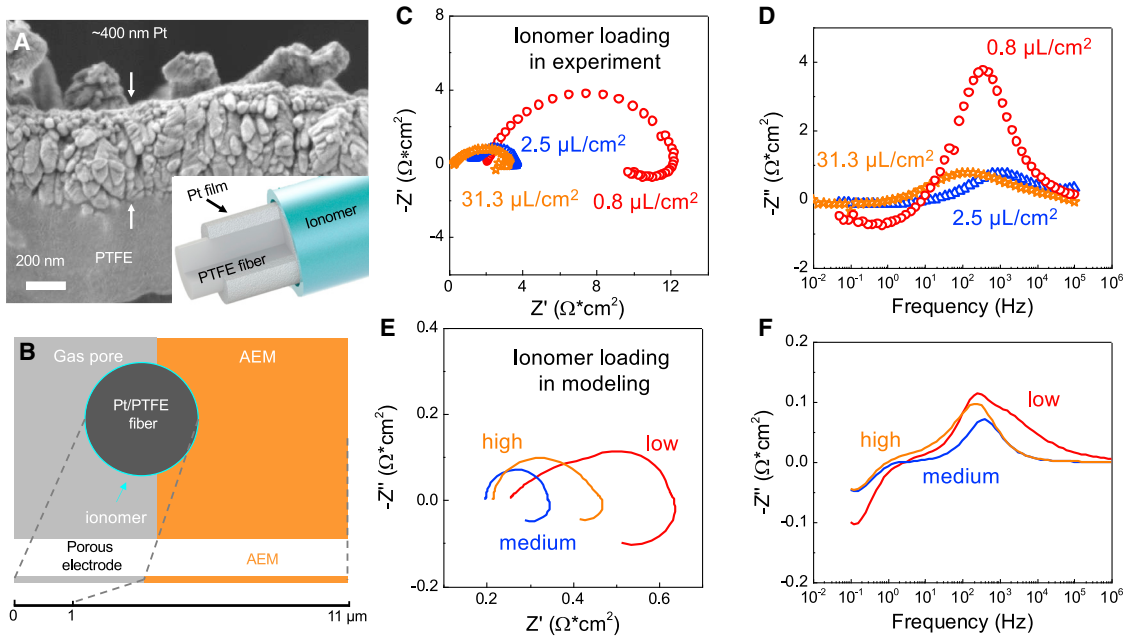

Figure 6. EIS of Pt/PTFE electrodes

(A–F) (A) Cross-sectioned SEM image of the Pt film (without ionomer) on the PTFE substrate. The inset shows a schematic of the cut-through view of the Pt/PTFE. (B) Schematics of the Pt/ionomer/PTFE fiber in a two-dimensional view, which can be simplified to a one-dimensional model, consisting of a porous electrode and an electrolyte segment. Comparison of (C) the experimental Nyquist and (D) Bode plot (at 0.75 V cell voltage), and (E and F) the corresponding modeled spectra (at −0.45 V overpotential, in model one where the oxygen concentration is fixed at x = 0), as a function of ionomer loading. (D and F) differ from conventional Bode plot, which has phase angle and overall impedance as y-axis. The oxygen concentration was fixed at the left boundary (x = 0). The effect of ionomer was assumed to increase the diffusion coefficient of OH^- but decrease that of oxygen in the porous electrode. Specifically, for low ionomer loading (low, red): $D_{OH^-} = 6 \times 10^{-12}\ m^2/s$, $D_{O_2} = 7.2 \times 10^{-5}\ m^2/s$, intermediate loading (medium, blue): $D_{OH^-} = 6 \times 10^{-10}\ m^2/s$, $D_{O_2} = 7.2 \times 10^{-9}\ m^2/s$, high loading (high, orange): $D_{OH^-} = 3 \times 10^{-9}\ m^2/s$, $D_{O_2} = 1.44 \times 10^{-10}\ m^2/s$.

(Figure 6E). The observed inductive loop also has important practical implications for AEMFCs, since it essentially decreases the real resistance at low-frequency ends, which corresponds to the slope in polarization curves and could contribute up to 15% to 30% performance improvement, as shown in PEMFCs.[30]

To study the effects of the ionomer loading on the mass transport, we compared the EIS spectra of the catalyst/PTFE fiber architecture at ionomer loadings of 0.8, 2.5, and 31.3 μL/cm^2. Overall, the spectra showed similar features of a higher frequency semicircle and a lower frequency inductive loop in the Nyquist plots (Figure 6C). The diameter of the capacitive semicircle decreases dramatically from 10.2 Ω*cm2 at ionomer loading 0.8 μL/cm^2 to 2.2 Ω*cm2 at 2.5 μL/cm^2, but increases again to 2.8 Ω*cm2 at 31.3 μL/cm^2. On the other hand, the inductive loop decreases monotonically as the ionomer loading increases.

To model the EIS spectra, increased ionomer loading is expected to improve the ionic conductivity within the porous electrode, but decrease the gas diffusion by filling the pores and blocking the accessible PTFE fibers that are highly permeable to oxygen gas. The experimental trends can thus be reproduced in model one by simultaneously adjusting the diffusion coefficients of oxygen D_{O_2} and hydroxide D_{OH^-} (Figure 6E). The capacitive arc decreases to a minimum value at medium ionomer loading and increases afterward at high loading. The peak positions of the capacitive semicircle locate at 251 (low loading), 398 (medium loading), and 199 Hz (high loading) (Figure 6F). The trend in peak shift is consistent with experimental results at 360 (low 0.8 μL/cm^2), 1,177 (medium

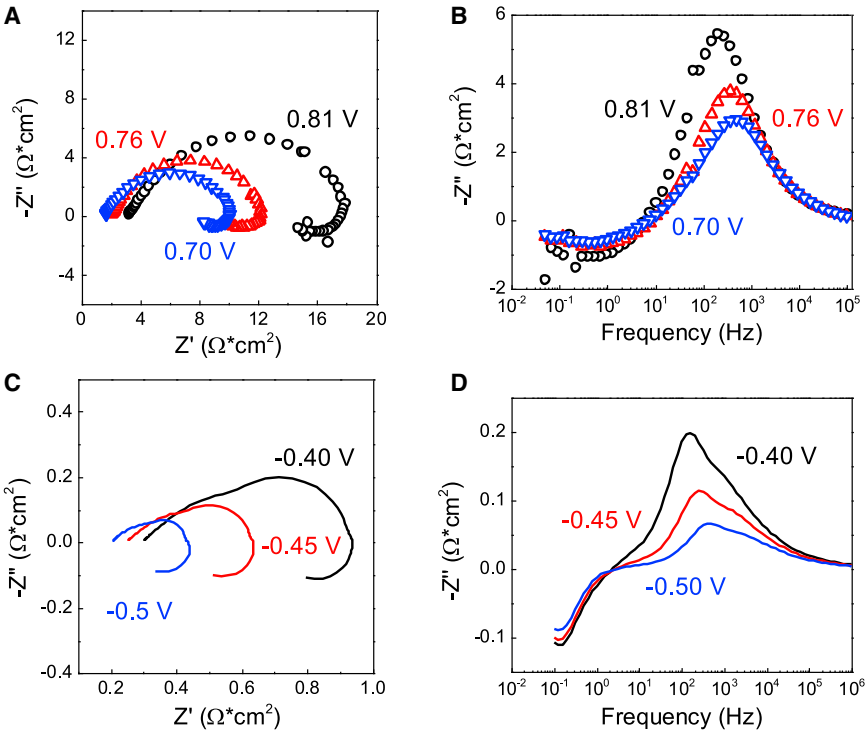

Figure 7. Modeling of EIS data

(A–D) Nyquist and Bode plots of (A and B) experimental EIS (0.8 μL/cm^2 ionomer loading) and (C and D) simulated spectra, at different overpotentials. Smaller cell potential in (A and B) means larger ORR overpotential, while more negative values indicate larger reaction overpotential in (C and D) because the thermodynamic potential is set to 0 V. The overall trend of the simulated spectra is consistent with the experimental results. Experimental testing conditions are the same as in Figure 4. In the simulation, $D_{OH^-} = 6 \times 10^{-12}\ m^2/s$, $D_{O_2} = 7.2 \times 10^{-5}\ m^2/s$, correspond to the low ionomer loading case in Figure 6E.

2.5 μL/cm^2), and 138 Hz (high 31.3 μL/cm^2) (Figure 6D). The smaller changes of peak position in the modeled results might be related to the use of diffusion and kinetic parameters that are not reliably known. It is noted that the experimental trends cannot be accounted for by adjusting only one of D_{O_2} and D_{OH^-} while keeping the other one constant (Figure S11). The capacitive peak position shifts monotonically to lower frequencies only if D_{O_2} was decreased as more ionomer was added (Figure S11B). Similarly, monotonic shifting to higher frequencies was observed only if D_{OH^-} was increased at higher ionomer loading (Figure S11D). The experimental Bode plot shows peak shifting to higher and lower frequencies at low (<2.5 μL/cm^2) and high (>2.5 μL/cm^2) ionomer loadings, respectively, indicating the dominant role of ionic and gaseous transport in the respective scenario. The extra shoulder at ~ 2k Hz in the modeled Bode plot for low ionomer loading can be attributed to the reaction resistance (Figure 6F). Experimental and modeled Nyquist and Bode plots at various applied overpotentials also show reasonable agreement, given the simplicity of the model (Figure 7). The capacitive arc decreases and shifts toward higher frequencies with increased overpotential, while that of the inductive loop stays at around the same frequency. The modeled steady-state polarization curves were also found to be dependent on ionomer loadings (Figure S12).

The origin of the inductive loop in the EIS spectra has been discussed in PEMFCs[30–33] and AEMFCs.[26,34] The essence of an inductive loop is negative resistance at lower

frequencies, which can happen in various ways. Two common reasons for the inductive loop are water transport and the presence of intermediate species in the ORR. In the former case, increased water production at higher current densities causes the resistance of the membrane and ionomer to drop if the frequency is low enough to allow the membrane to absorb the generated water.[33] For the latter, the resistance of a reaction usually contributes a frequency-independent term in the overall impedance, which gives rise to a capacitive semicircle when combined with an interfacial capacitor. This scenario changes when there is a time lag between the application of driving force and the resulting kinetic current, due to the involvement of surface absorbed intermediates.[35] An inductive loop is generated if the relaxation of the intermediate's coverage in response to the driving force is slow (and thus does not sync with the driving force, i.e., not a pure resistor) and leads to decreased overall resistance. This is the plausible mechanism for the inductive loop in alkaline ORR,[26,34] since the ORR is assumed to proceed through an ECE mechanism with the rate-limiting step (see the supplemental experimental procedures):

$$(O_2)_{ad} + H_2O + e^- \xrightarrow{k_b} O_2H_{ad} + OH^-$$

This reaction involves two surface-bound intermediates, O_2H_{ad} and OH_{ad}, which could generate an inductive loop, as described above. In our model, the inductive feature was also affected by both ionic and gaseous transport processes (Figure 6F), which change the relative phase of reaction intermediates. The rate constant of this step is found to affect the EIS spectra dramatically (Figure S13), with larger k_b leading to much smaller overall resistance.

The mechanisms of water transport and ORR reaction intermediates could be operative simultaneously in PEMFCs.[30] However, the inductive behavior could be masked by mass transport.[26] This situation was modeled by fixing the concentration of oxygen gas at the open boundary of AEM (see supplemental experimental procedures). To mimic the conventional catalyst layer at high ionomer loading, the AEM thickness was decreased to 10 nm to represent the ionomer layer around the Pt/C agglomerates (Figure 3B). In this case, only capacitive semicircles are observed, and the inductive feature due to the kinetic effect is absent due to the diffusion resistance through the bulk polyelectrolyte (Figure S14). The overall feature is independent of the AEM/ionomer thickness. Interestingly, the inductive loop was recovered by increasing the oxygen diffusion coefficient inside the AEM/ionomer (Figure S15). Finally, to gauge if the QAPPT ionomer can introduce gas transport resistance at ionomer coverage considered in this study, we deposited an extra layer of ionomer film onto a catalyst layer on a glassy carbon RDE, which was subsequently tested for the ORR in aqueous solution. Even though the transport mechanism could be different from that in the MEA, RDE measurements of the ORR revealed similar gaseous transport resistance under both acidic[36] and alkaline conditions.[37] The limiting current density decreases with higher ionomer loading (and with thicker ionomer films) (Figure S16), which could be explained by a blocking effect of the ionomer film on oxygen transport in the aqueous environment. It is noted that this result might also be caused by a decrease in activity of the catalytic sites, i.e., by a poisoning effect, because of the extra ionomer film.

Fuel cell performance tests (Figure 5), and the comparison between experimental and modeled EIS spectra (Figure 6 and S11) suggest different transport constraints for the low and high ends of ionomer loadings. Sluggish ionic transport is expected with minimal amounts of ionomer, 0 and 0.8 $\mu L/cm^2$. Excessive ionomer loadings, 10.4 and 31.3 $\mu L/cm^2$, mainly inhibit the diffusion of oxygen gas, possibly by

blocking the pores in the Pt/PTFE electrode. Model one was able to reproduce the trends of increased ionomer loading by simultaneously lowering D_{O_2} and increasing OH^- (Figure 6). In comparison, neither one of the effects alone can fully replicate the experimental data (Figure S11). We note that even though the model was able to reproduce the overall experimental trends, the absolute impedance values are about one order of magnitude different from the experimental ones (Figure 6E). This is partially due to the lack of reliable physiochemical property measurements on the AEM/ionomers used for AEMFCs. For this reason, the ionomer was treated only implicitly in our model by rendering the porous electrode ionically conducting and imposing a gas blocking effect. Models with explicit treatment of ionomer films have been reported, which can describe the gas exchange rate at the gas/ionomer interface. This exchange rate has been speculated to be the main gas transport resistance in traditional PEMFC MEA designs.[38,39] This approach is possible for a Nafion ionomer in PEMFCs since the effects of various factors such as thickness, humidity, and morphology on the behavior of Nafion have been well studied. Explicitly incorporating AEM ionomers into our model will require more data on the physiochemical properties of the QAPPT ionomer.

The unique advantage of the catalyst/PTFE fiber design is that it offers easier control over the organization of the catalyst and ionomer, and thus the study of the effects of microstructure on mass transport and fuel cell performance. In particular, the thickness of the catalyst and ionomer film can be easily adjusted and characterized, which would be further assisted by higher dimensional models that incorporate these structural features. For instance, modeling of a single fiber in the three-dimensional domain with explicit ionomer would integrate factors such as surface gas exchange and water liquid-vapor equilibrium.

We note that the fuel cell performance of our current Pt/PTFE fiber design cannot rival that of the best AEMFCs reported so far. The performance of AEMFCs depends on various factors, including catalyst composition and loading, type of ionomers, water management, gas flow rate, and temperature. For example, Kohl et al reported 3.5 W/cm^2 peak power density for AEMFCs using slightly crosslinked AEMs that can made as thin as 10 μm.[6,8] Wang et al. reported the design of poly (aryl piperidinium) AEM that achieves peak power density of 920 mW/cm^2,[7] similar to the performance of the AEM/ionomer used for this study in the conventional MEA configuration.[4] The performance of the Pt/PTFE fiber architecture may be improved by using fiber supports with higher surface area. The catalyst loading in the current design is high compared with that of conventional MEAs but could be lowered by co-sputtering conductive substrates and thin catalyst films. An especially interesting finding is that the Ag/PTFE electrode reaches a high current density (~1 A/cm^2) without added ionomer, indicating the possible role of the Ag surface as an effective ion conductor. This point deserves further study and is currently being pursued in our group. The large activation overpotential (~0.38 V, Figure 4C) at lower current densities could potentially be mitigated by employing alloyed catalysts with higher activities.[40]

DISCUSSION

In summary, we have studied mass transport in conventional MEA geometries and PTFE fiber-based architectures for AEMFCs. Understanding mass transport in the MEA configuration is facilitated by designing a PTFE fiber-based ORR electrode that is more amenable to finite element modeling because new architecture allows for easier control and characterization of the microstructures. This design employs a

porous PTFE membrane sputtered with a thin Ag or Pt film as the catalyst layer. The ionomer loading was found to affect the mass transport significantly and thus the fuel cell performance. Assisted by EIS and numerical modeling tools, the transport of ions and gases were shown to limit the cathode performance at lower and higher ionomer loadings, a trend that was also found for the conventional catalyst layers. This result suggests that more gas-permeable alkaline ionomers would be more effective in AEMFCs, as has been demonstrated in PEMFCs.[19] While the initial results of using the catalyst/PTFE fiber architecture in alkaline fuel cells are encouraging, future efforts are still needed to improve the design by lowering the catalyst loading, increasing the catalytic activity, and optimizing the substrate porosity. Compared with the conventional MEA configuration, the fiber architecture offers better control over the microstructure in the catalyst layer, which will be beneficial for studying ion and molecule transport in gas-fed electrochemical devices.

EXPERIMENTAL PROCEDURES

Resource availability

Lead contact

Further information and requests for resources should be directed to and will be fulfilled by the lead contact, Thomas E. Mallouk (mallouk@sas.upenn.edu).

Materials availability

The materials described in this study, except those obtained from commercial sources or third parties, can be made available upon request.

Data and code availability

Data related to this study are provided in this article and the supplemental information. Additional data are available from the lead contact upon reasonable request.

Materials and methods

Pt/C and PtRu/C nanoparticles (60 wt%, on HAS Ketjenblack), Nafion dispersion (D521, 5 wt%), and carbon paper with microporous layer were purchased from the FuelCell Store. PTFE membrane filters (aspire laminated, hydrophobic, polypropylene backer, 0.1 micron) were purchased from Sterlitech. AEMs and ionomers (aQAPPT, Cl^- as counter ion) were the same as reported in previous papers.[4] The AEM/ionomer, quaternary ammonia poly (N-methyl-piperidine-co-p-terphenyl) has a structure shown in Figure 1C, with cation remaining degree and ion exchange capacity of 95.9 and 2.36 mmol/g, respectively (in 1 M NaOH). Fuel cell hardware and the fuel cell test stand (850e, multi-range) were purchased from Scribner Associates. All other chemicals were received from Sigma-Aldrich and were used without additional purification.

Fuel cell tests

For fuel cell tests in the conventional MEA configuration, procedures from previous literature reports were followed.[4] Pt/C and PtRu/C powders (60 wt%, 6 mg) and 75 μL AEM ionomer (2 wt% in DMSO) were added to 1.5 mL 1-propanol (18.8 $\mu L/cm^2$ ionomer loading, catalyst/ionomer ratio: 4:1). To study the effect of ionomer loading, 30 μL of ionomer was added to the catalyst ink, corresponding to 7.5 $\mu L/cm^2$ ionomer loading (catalyst/ionomer mass ratio of 10:1). The mixture was sonicated in a bath sonicator (Branson 5510) for 1 h to obtain a uniform catalyst ink. The prepared ink was sprayed onto a piece of AEM (QAPPT 35 μm, 3 cm by 3 cm), which was held flat by a heated vacuum table at ~60°C. The active area (2 cm × 2 cm) was set by a window cut into a PTFE mask. The spraying process was accomplished by a spraying gun (Master Airbrush, G233) attached to a modified 3D printer (Creality, Ender) that

fixes the gun ~2 cm above the membrane and controls the motion in the X-Y directions. Pt/C and PtRu/C were sprayed onto the two sides of the AEM and served as the cathode and anode electrodes, respectively. The metal loading was determined to be ~0.4 mg/cm^2. The catalyst-coated membrane (CCM) was activated in 1 M KOH (99.98% purity) solution in a 70°C oven overnight to replace the Cl^- with OH^-. The activated CCM was thoroughly rinsed with deionized water before the fuel cell test.

For fuel cells with the novel architectures discussed in the main text, only one side of the AEM was covered with PtRu/C as the anode electrode. The cathode was fabricated by sputtering Ag or Pt films onto the PTFE substrate at a ~0.1 nm/s sputtering rate with a sputtering tool. Approximately 400 nm nominal thickness was used for Pt and Ag samples. The Pt/PTFE samples were further modified by spraying AEM or Nafion ionomers. The target amount of ionomer (for example, 75 μL 2 wt% AEM ionomer, or 30 μL 5 wt% Nafion) was dispersed in 0.5 mL 1-propanol. The mixture was sprayed onto the Pt films with a window mask that gave a geometric area of ~2 cm by 1.2 cm. More details of the fuel cell testing are provided in the supplemental experimental procedures.

EIS spectra at high current densities were taken using the frequency response analyzer built into the fuel cell test stand. The frequency range was 0.1 Hz–5000 Hz. The amplitude of the AC current was taken to be 5% of the applied DC current. For lower current densities, the EIS spectra were obtained with the Autolab (128 N or 301 N, Metrohm) in the potentiostatic mode.

Characterization

SEM images and energy dispersive spectroscopy (EDX) were performed using a ZEISS Gemini 500 SEM. SEM images were acquired at 1 kV and EDX spectra were acquired at 30 kV and 38 nA to maximize the X-ray signal output for elemental quantification while maintaining reasonable spatial resolution for elemental mapping. The ionomer coverage in the conventional catalyst layer was characterized by cryo-TEM. A catalyst/ionomer ink mixture of Pt/C catalyst and QAPPT ionomer was drop-cast directly onto a lacey carbon support film copper grid. These grids were then heated for 12 h at 80°C and ~1e-6 mbar to remove any dimethyl sulfoxide (DMSO) solvent from the catalyst/ionomer mixture. Imaging was done on a Thermo Fisher Talos Arctica TEM operating at an acceleration voltage of 200 kV at −190°C. In order to preserve the ionomer and avoid radiation degradation, the total dose applied to the sample remained below 200 e Å^{-2}.

Numerical modeling

All modeling was done using COMSOL v5.6. The geometry of the Pt/PTFE cathode has a relatively simple structure that could be captured by a one-dimensional model (Figure 6B). The model consists of a 1-μm porous electrode and a 10-μm-thick electrolyte region. A mesh size of 0.01 nm was used at the boundaries, and the relative tolerance was set to 10^{-4}. The EIS spectra were obtained using frequency domain perturbation, where the frequency-domain form of the governing equations for all species (O_2, OH^-, and K^+) was solved for. A step size of 0.1 was used for EIS modeling (Figure S10). More details of the model description and simulation parameters are available in the supplemental information.

SUPPLEMENTAL INFORMATION

Supplemental information can be found online at https://doi.org/10.1016/j.xcrp.2022.100912.

ACKNOWLEDGMENTS

This work was supported by the Center for Alkaline-Based Energy Solutions, an Energy Frontier Research Center program supported by the US Department of Energy, under Grant DE-SC0019445. This work made use of the Cornell Center for Materials Research Shared Facilities, which are supported through the NSF MRSEC program (DMR-1719875). We thank Professor Lin Zhuang's group at Wuhan University for providing the QAPPT membrane and ionomer.

AUTHOR CONTRIBUTIONS

Z.Y., L.F.K., H.D.A., and T.E.M. designed the study. Z.Y. carried out fuel cell tests and numerical modeling with assistance from J.L.H. and A.V. M.C. and Y.Y. carried out the Cryo-EM and SEM characterization and analysis. J.M.M. assisted with sample preparations. Z.Y. and T.E.M. drafted the manuscript, which was reviewed and edited by all authors.

DECLARATION OF INTERESTS

The authors declare no competing interests.

Received: September 13, 2021
Revised: April 14, 2022
Accepted: May 5, 2022
Published: May 30, 2022

REFERENCES

1. Lewis, N.S., and Nocera, D.G. (2006). Powering the planet: chemical challenges in solar energy utilization. Proc. Natl. Acad. Sci. U S A *103*, 15729–15735. https://doi.org/10.1073/pnas.0603395103.

2. Yan, Z., Hitt, J.L., Turner, J.A., and Mallouk, T.E. (2019). Renewable electricity storage using electrolysis. Proc. Natl. Acad. Sci. U S A *117*, 12558–12563. https://doi.org/10.1073/pnas.1821686116.

3. Wang, Y., Yang, Y., Jia, S., Wang, X., Lyu, K., Peng, Y., Zheng, H., Wei, X., Ren, H., Xiao, L., et al. (2019). Synergistic Mn-Co catalyst outperforms Pt on high-rate oxygen reduction for alkaline polymer electrolyte fuel cells. Nat. Commun. *10*, 1506. https://doi.org/10.1038/s41467-019-09503-4.

4. Peng, H., Li, Q., Hu, M., Xiao, L., Lu, J., and Zhuang, L. (2018). Alkaline polymer electrolyte fuel cells stably working at 80 °C. J. Power Sources *390*, 165–167. https://doi.org/10.1016/j.jpowsour.2018.04.047.

5. Ul Hassan, N., Mandal, M., Huang, G., Firouzjaie, H.A., Kohl, P.A., and Mustain, W.E. (2020). Achieving high-performance and 2000 h stability in anion exchange membrane fuel cells by manipulating ionomer properties and electrode optimization. Adv. Energy Mater *10*, 2001986. https://doi.org/10.1002/aenm.202001986.

6. Huang, G., Mandal, M., Peng, X., Yang-Neyerlin, A.C., Pivovar, B.S., Mustain, W.E., and Kohl, P.A. (2019). Composite poly(Norbornene) anion conducting membranes for achieving durability, water management and high Power (3.4 W/cm^2) in hydrogen/oxygen alkaline fuel cells. J. Electrochem. Soc. *166*, F637–F644. https://doi.org/10.1149/2.1301910jes.

7. Wang, J., Zhao, Y., Setzler, B.P., Rojas-Carbonell, S., Ben Yehuda, C., Amel, A., Page, M., Wang, L., Hu, K., Shi, L., et al. (2019). Poly(aryl piperidinium) membranes and ionomers for hydroxide exchange membrane fuel cells. Nat. Energy *4*, 392–398. https://doi.org/10.1038/s41560-019-0372-8.

8. Mandal, M., Huang, G., Hassan, N.U., Peng, X., Gu, T., Brooks-Starks, A.H., Bahar, B., Mustain, W.E., and Kohl, P.A. (2020). The importance of water transport in high conductivity and high-power alkaline fuel cells. J. Electrochem. Soc. *167*, 054501. https://doi.org/10.1149/2.0022005JES.

9. Weber, A.Z., and Newman, J. (2004). Modeling transport in polymer-electrolyte fuel cells. Chem. Rev. *104*, 4679–4726. https://doi.org/10.1021/cr020729l.

10. Weber, A.Z., Borup, R.L., Darling, R.M., Das, P.K., Dursch, T.J., Gu, W., Harvey, D., Kusoglu, A., Litster, S., Mench, M.M., et al. (2014). A critical review of modeling transport phenomena in polymer-electrolyte fuel cells. J. Electrochem. Soc. *161*, F1254–F1299. https://doi.org/10.1149/2.0751412jes.

11. Nonoyama, N., Okazaki, S., Weber, A.Z., Ikogi, Y., and Yoshida, T. (2011). Analysis of oxygen-transport diffusion resistance in proton-exchange-membrane fuel cells. J. Electrochem. Soc. *158*, B416. https://doi.org/10.1149/1.3546038.

12. O'Hayre, R., and Prinz, F.B. (2004). The air/platinum/nafion triple-phase boundary: characteristics, scaling, and implications for fuel cells. J. Electrochem. Soc. *151*, A756. https://doi.org/10.1149/1.1701868.

13. Brown, E.C., Wilke, S.K., Boyd, D.A., Goodwin, D.G., and Haile, S.M. (2010). Polymer sphere lithography for solid oxide fuel cells: a route to functional, well-defined electrode structures. J. Mater. Chem. *20*, 2190. https://doi.org/10.1039/b920973e.

14. Yarlagadda, V., Carpenter, M.K., Moylan, T.E., Kukreja, R.S., Koestner, R., Gu, W., Thompson, L., and Kongkanand, A. (2018). Boosting fuel cell performance with accessible carbon mesopores. ACS Energy Lett *3*, 618–621. https://doi.org/10.1021/acsenergylett.8b00186.

15. Page, K.A., Kusoglu, A., Stafford, C.M., Kim, S., Kline, R.J., and Weber, A.Z. (2014). Confinement-driven increase in ionomer thin-film modulus. Nano Lett. *14*, 2299–2304. https://doi.org/10.1021/nl501233g.

16. Paul, D.K., Fraser, A., and Karan, K. (2011). Towards the understanding of proton conduction mechanism in PEMFC catalyst layer: conductivity of adsorbed Nafion films. Electrochem. Commun. *13*, 774–777. https://doi.org/10.1016/j.elecom.2011.04.022.

17. Kongkanand, A., and Mathias, M.F. (2016). The priority and challenge of high-power performance of low-platinum proton-exchange membrane fuel cells. J. Phys. Chem. Lett. *7*, 1127–1137. https://doi.org/10.1021/acs.jpclett.6b00216.

18. Lopez-haro, M., Guétaz, L., Printemps, T., Morin, A., Escribano, S., Jouneau, P.H., Bayle-guillemaud, P., Chandezon, F., and Gebel, G. (2014). Three-dimensional analysis of Nafion

layers in fuel cell electrodes. Nat. Commun. *5*, 5229. https://doi.org/10.1038/ncomms6229.

19. Kinoshita, S., Tanuma, T., Yamada, K., Hommura, S., Watakabe, A., Saito, S., and Shimohira, T. (2014). (Invited) development of PFSA ionomers for the membrane and the electrodes. ECS Trans. *64*, 371–375. https://doi.org/10.1149/06403.0371ecst.

20. Cetinbas, F.C., Ahluwalia, R.K., Kariuki, N.N., De Andrade, V., and Myers, D.J. (2019). Effects of porous carbon morphology, agglomerate structure and relative humidity on local oxygen transport resistance. J. Electrochem. Soc. *167*, 013508. https://doi.org/10.1149/2.0082001JES.

21. Padgett, E., Andrejevic, N., Liu, Z., Kongkanand, A., Gu, W., Moriyama, K., Jiang, Y., Kumaraguru, S., Moylan, T.E., Kukreja, R., and Muller, D.A. (2018). Editors' choice—connecting fuel cell catalyst nanostructure and accessibility using quantitative cryo-STEM tomography. J. Electrochem. Soc. *165*, F173–F180. https://doi.org/10.1149/2.0541803jes.

22. Debe, M.K., Schmoeckel, A.K., Vernstrom, G.D., and Atanasoski, R. (2006). High voltage stability of nanostructured thin film catalysts for PEM fuel cells. J. Power Sourc. *161*, 1002–1011. https://doi.org/10.1016/j.jpowsour.2006.05.033.

23. García de Arquer, F.P., Dinh, C.-T., Ozden, A., Wicks, J., McCallum, C., Kirmani, A.R., Nam, D.-H., Gabardo, C., Seifitokaldani, A., Wang, X., et al. (2020). CO_2 electrolysis to multicarbon products at activities greater than 1 A/cm^2. Science *367*, 661–666. https://doi.org/10.1126/science.aay4217.

24. Wicks, J., Jue, M.L., Beck, V.A., Oakdale, J.S., Dudukovic, N.A., Clemens, A.L., Liang, S., Ellis, M.E., Lee, G., Baker, S.E., et al. (2021). 3D-printable fluoropolymer gas diffusion layers for CO_2 electroreduction. Adv. Mater. *33*, 2003855. https://doi.org/10.1002/adma.202003855.

25. Reshetenko, T., Odgaard, M., Schlueter, D., and Serov, A. (2018). Analysis of alkaline exchange membrane fuel cells performance at different operating conditions using DC and AC methods. J. Power Sourc. *375*, 185–190. https://doi.org/10.1016/j.jpowsour.2017.11.030.

26. Genies, L., Bultel, Y., Faure, R., and Durand, R. (2003). Impedance study of the oxygen reduction reaction on platinum nanoparticles in alkaline media. Electrochimica Acta *48*, 3879–3890. https://doi.org/10.1016/S0013-4686(03)00525-5.

27. Ripatti, D.S., Veltman, T.R., and Kanan, M.W. (2019). Carbon monoxide gas diffusion electrolysis that produces concentrated C2 products with high single-pass conversion. Joule *3*, 240–256. https://doi.org/10.1016/j.joule.2018.10.007.

28. Sheng, W., Gasteiger, H.A., and Shao-Horn, Y. (2010). Hydrogen oxidation and evolution reaction kinetics on platinum: acid vs alkaline electrolytes. J. Electrochem. Soc. *157*, B1529. https://doi.org/10.1149/1.3483106.

29. Yang, Y., Peltier, C.R., Zeng, R., Schimmenti, R., Li, Q., Huang, X., Yan, Z., Potsi, G., Selhorst, R., Lu, X., et al. (2022). Electrocatalysis in alkaline media and alkaline membrane-based energy technologies. Chem. Rev. *122*, 6117–6321. https://doi.org/10.1021/acs.chemrev.1c00331.

30. Schiefer, A., Heinzmann, M., and Weber, A. (2020). Inductive low-frequency processes in PEMFC-impedance spectra. Fuel Cells *20*, 499–506. https://doi.org/10.1002/fuce.201900212.

31. Pivac, I., and Barbir, F. (2016). Inductive phenomena at low frequencies in impedance spectra of proton exchange membrane fuel cells – a review. J. Power Sourc. *326*, 112–119. https://doi.org/10.1016/j.jpowsour.2016.06.119.

32. Pivac, I., Šimić, B., and Barbir, F. (2017). Experimental diagnostics and modeling of inductive phenomena at low frequencies in impedance spectra of proton exchange membrane fuel cells. J. Power Sourc. *365*, 240–248. https://doi.org/10.1016/j.jpowsour.2017.08.087.

33. Setzler, B.P., and Fuller, T.F. (2015). A physics-based impedance model of proton exchange membrane fuel cells exhibiting low-frequency inductive loops. J. Electrochem. Soc. *162*, F519–F530. https://doi.org/10.1149/2.0361506jes.

34. Itagaki, M., Hasegawa, H., Watanabe, K., and Hachiya, T. (2003). Electroreduction mechanism of oxygen investigated by electrochemical impedance spectroscopy. J. Electroanal. Chem. *557*, 59–73. https://doi.org/10.1016/S0022-0728(03)00349-8.

35. Klotz, D. (2019). Negative capacitance or inductive loop? – a general assessment of a common low frequency impedance feature. Electrochem. Commun. *98*, 58–62. https://doi.org/10.1016/j.elecom.2018.11.017.

36. Ignaszak, A., Ye, S., and Gyenge, E. (2009). A study of the catalytic interface for O_2 electroreduction on Pt: the interaction between carbon support meso/microstructure and ionomer (Nafion) distribution. J. Phys. Chem. C *113*, 298–307. https://doi.org/10.1021/jp8060398.

37. Santori, P.G., Mondal, A.N., Dekel, D.R., and Jaouen, F. (2020). The critical importance of ionomers on the electrochemical activity of platinum and platinum-free catalysts for anion-exchange membrane fuel cells. Sustain. Energy Fuels *4*, 3300–3307. https://doi.org/10.1039/D0SE00483A.

38. Owejan, J.P., Owejan, J.E., and Gu, W. (2013). Impact of platinum loading and catalyst layer structure on PEMFC performance. J. Electrochem. Soc. *160*, F824–F833. https://doi.org/10.1149/2.072308jes.

39. Greszler, T.A., Caulk, D., and Sinha, P. (2012). The impact of platinum loading on oxygen transport resistance. J. Electrochem. Soc. *159*, F831–F840. https://doi.org/10.1149/2.061212jes.

40. Holewinski, A., Idrobo, J.-C., and Linic, S. (2014). High-performance Ag–Co alloy catalysts for electrochemical oxygen reduction. Nat. Chem. *6*, 828–834. https://doi.org/10.1038/nchem.2032.